

Featuring research from the Breast Cancer Research Program of Professor Sofia D. Merajver at the University of Michigan.

A platform for artificial intelligence based identification of the extravasation potential of cancer cells into the brain metastatic niche

A new platform for detecting cancer cells with a brain metastatic phenotype. This approach combines artificial intelligence, a blood brain barrier on a chip and confocal tomography to discern between the metastatic signatures of cancer cells, and may lead to new treatment modalities.

As featured in:



See Sofia D. Merajver et al., *Lab Chip*, 2019, 19, 1162.



ROYAL SOCIETY
OF CHEMISTRY

Celebrating
IYPT 2019

rsc.li/loc

Registered charity number: 207890



Cite this: *Lab Chip*, 2019, 19, 1162

A platform for artificial intelligence based identification of the extravasation potential of cancer cells into the brain metastatic niche†

C. Ryan Oliver,[‡] Megan A. Altemus,[‡] Trisha M. Westerhof,[‡] Hannah Cheriyan,^a Xu Cheng,^a Michelle Dziubinski,[‡] Zhifen Wu,^a Joel Yates,^a Aki Morikawa,^a Jason Heth,^c Maria G. Castro,^{cd} Brendan M. Leung,[§] Shuichi Takayama,[¶] and Sofia D. Merajver^{*a}

Brain metastases are the most lethal complication of advanced cancer; therefore, it is critical to identify when a tumor has the potential to metastasize to the brain. There are currently no interventions that shed light on the potential of primary tumors to metastasize to the brain. We constructed and tested a platform to quantitatively profile the dynamic phenotypes of cancer cells from aggressive triple negative breast cancer cell lines and patient derived xenografts (PDXs), generated from a primary tumor and brain metastases from tumors of diverse organs of origin. Combining an advanced live cell imaging algorithm and artificial intelligence, we profile cancer cell extravasation within a microfluidic blood–brain niche (μ BBN) chip, to detect the minute differences between cells with brain metastatic potential and those without with a PPV of 0.91 in the context of this study. The results show remarkably sharp and reproducible distinction between cells that do and those which do not metastasize inside of the device.

Received 19th December 2018,
Accepted 15th February 2019

DOI: 10.1039/c8lc01387j

rs.c.li/loc

Introduction

Brain metastatic spread of cancer is the most lethal event in cancer progression. Approximately 15% of all breast cancer patients develop a brain metastatic lesion, making it the most frequent tissue of origin of brain metastases in women. Brain metastases as a result of breast cancer are increasing in incidence due to improved imaging technologies leading to increased detection and better primary tumor management which allows more time for metastases to develop.^{1–5} While there have been significant advances in the development of targeted therapies for some metastatic breast cancers (e.g. anti-estrogen and anti-HER2 drugs), systemic therapy cur-

rently has a limited role in the treatment of brain metastasis.⁶ Moreover, there is a lack of predictive tools with clinically relevant metrics to predict if subpopulations of the patient's primary tumor cells will metastasize to the brain. Because of these challenges, we propose a platform which could be used in a precision medicine approach to identify the likelihood of brain metastases arising from primary lesions. We posed that artificial intelligence could identify cancer cells which exhibited a brain metastatic phenotype using accurate 3D measurement of their behavior in an *ex vivo* BBB model (Fig. 1).⁷

Three-dimensional measurement of each cancer cell in a live patient's tumor micro-environment would be ideal. However, current technology such as MRI is unable to meet this need because it is both expensive and lacks single cell fidelity (0.2 mm \times 0.2 mm \times 1.2 mm resolutions for 7 Tesla MRI from Siemens specification sheet). Therefore, the current practice is to biopsy the suspected tumor and a pathologist scans individual slices from the sample, each layer only a few microns thick.⁸ An experienced pathologist can identify cancers and even cancer cells with reasonable accuracy.⁹ However, it is tedious and there is a large variation among pathologist based on experience.¹⁰ Moreover, this approach is focused on the question of identifying a tumor or metastasis already grown and present at the biopsy location. There is no method to identify the probability of a cell to migrate across the patient's blood brain barrier in the future. It is unknown

^a Department of Internal Medicine, University of Michigan, Ann Arbor, MI 48109, USA. E-mail: smerajve@umich.edu

^b Department of Biomedical Engineering, University of Michigan, Ann Arbor, MI 48109, USA

^c Department of Neurosurgery, University of Michigan, Ann Arbor, MI 48109, USA

^d Department of Cell and Developmental Biology, University of Michigan, Ann Arbor, MI 48109, USA

† Electronic supplementary information (ESI) available. See DOI: 10.1039/c8lc01387j

‡ Equal contribution.

§ Current affiliation: Department of Applied Oral Sciences and School of Biomedical Engineering, Dalhousie University, Nova Scotia, Canada.

¶ Current affiliation: The Wallace H Coulter Department of Biomedical Engineering, Georgia Institute of Technology and Emory School of Medicine, Atlanta GA 30332, USA.

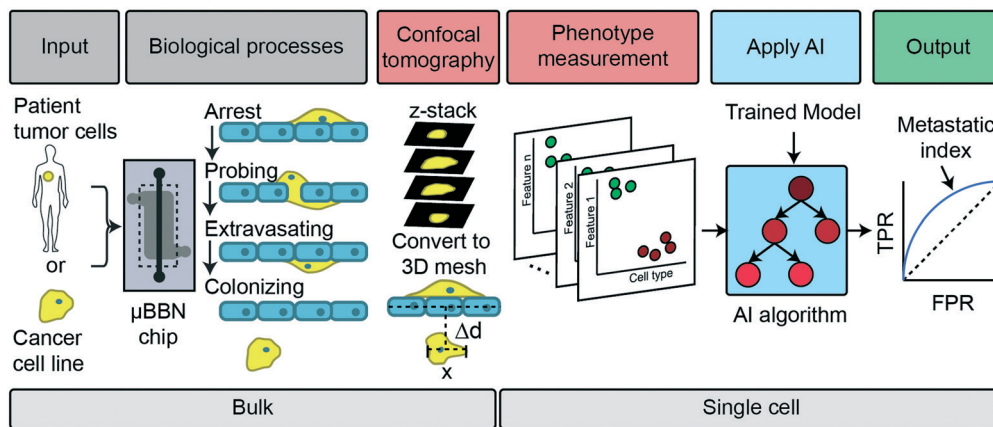


Fig. 1 Overview of method. The concept we demonstrate is to culture cells from a cell line or patient in an *in vitro* BBB device allowing the cancer cells to undergo late stage metastatic processes. The result is then imaged *via* confocal tomography after 24 and 48 h. The confocal z-stack is converted to a 3D mesh and single cell phenotypic measurements are calculated such as the distance from the endothelial layer and shape. The feature measurements are evaluated by a trained artificial intelligence (AI) model to determine if the cells have a high, medium, or low brain metastatic potential index.

how many cells in a tumor have this capacity, but it is thought to only be a small percentage, thus the importance of identifying them. It then follows that it is important to sample a large number of cells from the patient's tumor with high fidelity and reproducibility to detect minute differences that relate to the probability and potential to metastasize the brain.¹¹ Such a technical challenge indicates a need for methods to capture measurements of the morphologic phenotype of live cancer cells in 3D from an *ex vivo* micro-environment representing tissue to which they metastasize, such as the BBB. This approach differs from murine models which are largely slow to metastasize and whose brain micro-environments differ significantly from humans.^{12–14} We solve this challenge by the use of confocal imaging combined with mesh-based tomography of cancer cell phenotypes in a published BBB organ on a chip model.^{15–18}

Finally, the visual differences between cancer cells that can metastasize to the brain and those that cannot are subtle. Trained professionals may have difficulty telling them apart in many cases resulting in delayed treatment.⁹ It is known that treatment early in disease progression is critical to positive outcomes highlighting an opportunity for improvement.¹⁹ Artificial intelligence has already been shown to be effective in 2D pathology and we pose that if combined with 3D confocal tomography of an *ex vivo* blood brain barrier it could be trained to reliably identify the minute differences between cells with metastatic potential and those without.

Thus, in our approach (Fig. 1) we combine a BBB on a chip with advanced imaging software (confocal tomography) to improve the quantitation and reliability of the measurements of cellular dynamic phenotypes and features as the cells traverse the BBB (Fig. 2c and d). Using this platform, we characterize the migratory and proliferative phenotypes of cancer cells with varying degrees of brain metastatic potential as well as cells from cancer patient samples with known metastatic potential. These results when combined with artificial

intelligence (AI), lead to a model which can be used to predict the metastatic potential of cancer cells.

Results and discussion

Brain seeking breast cancer cell line reveals a distinct μ BBN phenotypic pattern

Having confirmed the endothelium's barrier function by small molecule exclusion and comparing it to previously published models (Fig. 2f and g), we profiled breast cancer cell behavior in the μ BBN device to identify important phenotypic features. After a confluent monolayer of hCMEC/D3-DsRed cells was established, GFP-expressing MDA-MB-231 cells (triple-negative breast cancer), MDA-MB-231-BR cells (brain-seeking subclone of MDA-MB-231), or MCF10A cells (normal-like breast epithelium) were seeded onto the top chamber. After 24 or 48 h, the entire μ BBN device was imaged *via* confocal microscopy (see Methods) (Fig. 2c–e) to measure the final stages in the metastatic cascade.

Fig. 3a and b show examples of diverse morphologies of representative cells in the device, by cell line, at 24 h and 48 h, respectively.²⁰ The four parametric variables chosen for this study were used to characterize the cancer cells behavior. Percent volume extravasated is the percentage (0–100%) of the cell's volume that has passed through the barrier plane. For this metric, MCF10A and MDA-MB-231 cells had a substantial proportion of cells that were less than 50% extravasated (59% and 57%, respectively). In contrast, the MDA-MB-231-BR had 32–35% greater proportion of cells >50% extravasated (Fig. 3c, Table S1†). After 48 h, unlike the MCF10A cells both cancer cell lines bulk populations had extravasated more than 50% (87% and 95%, respectively). However, only the MDA-MB-231-BR cells had a large sub-population 100% extravasated (14% compared to <1% for all other cell lines). The distribution of percent volume extravasated was statistically significantly different across all cell lines at both time

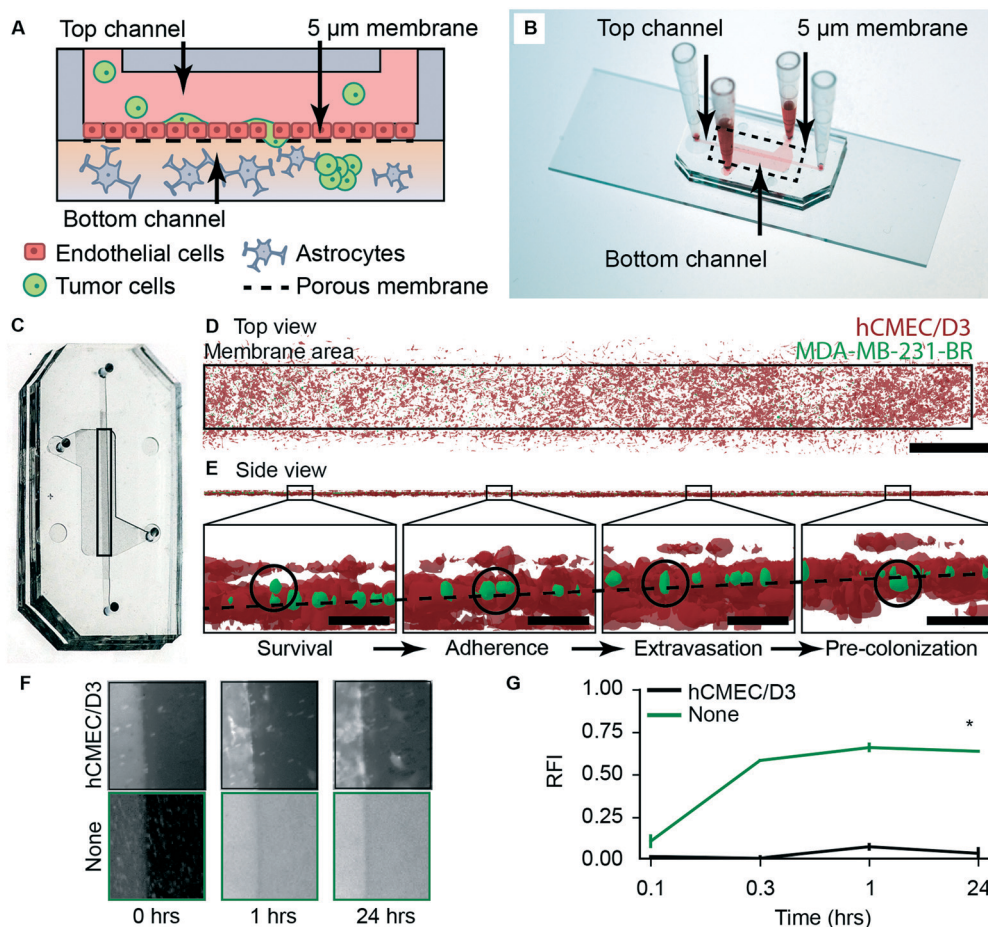


Fig. 2 Microfluidic BBNiche device design to study brain metastatic process. (A) Schematic of μ BBN device. (B) Image of the μ BBN device indicating top channel, bottom chamber, and porous membrane. (C) Confocal images of μ BBN device are analyzed using 3D rendered objects. hCMCE/D3 endothelial layer in μ BBN device forms a barrier between the top and bottom chambers. Image of the μ BBN from top of device showing the area being imaged (black rectangle). (D) 3D-rendered μ BBN device 24 h post-seeding with MDA-MB-231-BR cells from top-down. Scale bar = 1000 μ m. (E) Side view of the channel with insets showing cancer cells at various stages of traversing endothelium. Dashed line shows plane fit to the endothelium. Circles highlight representative cells. Scale bar = 200 μ m. (F) μ BBN device at 0, 1, and 24 h after addition of 10 kDa FITC-Dextran for device with hCMCE/D3 cells and device without. Black box indicates area of chip shown in images. (G) Quantification of permeability after addition of FITC-Dextran in devices with and without hCMCE/D3 layer. Values are the average of three areas per time point with $n = 3$ biological replicates. Error bars indicate standard deviation. * $p < 0.05$.

points according to a Kolmogorov-Smirnov test (all p -values $< 8 \times 10^{-5}$) (Table S1†).

Distance extravasated (Fig. 3c, Table S1†) is the distance in μ m between the center of a cell in the stromal chamber and the endothelial cell layer. One way to analyze the cellular behavior is by binning the distances the cells extravasated and studying the percentage of cells near or in the endothelium (Zone 1: < 50 μ m, green), migratory cells (Zone 2: > 50 – 100 μ m, yellow), and cells attracted to the astrocytes (Zone 3: > 100 μ m, red). At 24 h after seeding, all cancer cell lines tended to remain close to the plane in Zone 1 (MCF10A: 36%, MDA-MB-231: 26%, MDA-MB-231-BR: 74%). The cancer cell lines had 3-fold as many cells in Zone 2. However, at 48 h, a subpopulation of MDA-MB-231-BR cells (Zone 2: 11%, Zone 3: 12%) moved ~ 100 μ m into the bottom chamber (max = 190.6 μ m). Extravasated subpopulations are not observed in the parental MDA-MB-231 (1.6% in Zones 2–3) or

the normal-like MCF10A (0.3% in Zones 2–3). The distribution of distances cancer cells traversed differed significantly across all cell lines at both time points, by the Kolmogorov-Smirnov test (all p -values $< 8 \times 10^{-6}$) (Table S1†).

The morphologies of the cells in the device were quantified by the sphericity of cells extravasated, with 1.0 being the sphericity of a perfect sphere (Fig. 3e, Table S1†, eqn (1)) (see Methods). Sphericity is thought to be related to RhoA and RhoC expression and is a result of their role in migratory phenotypes. At 24 h, the MCF10A cells were least spherical (0.44), and the MDA-MB-231-BR cells were most spherical (0.73). Over 48 h post-seeding in the μ BBN chip, the distribution of sphericity of MCF10A (0.47) and MDA-MB-231 cells remained approximately the same, while the MDA-MB-231-BR cells became less spherical (0.52).

The cell populations detected within the device were separated into two subsets to assess if the extravasated

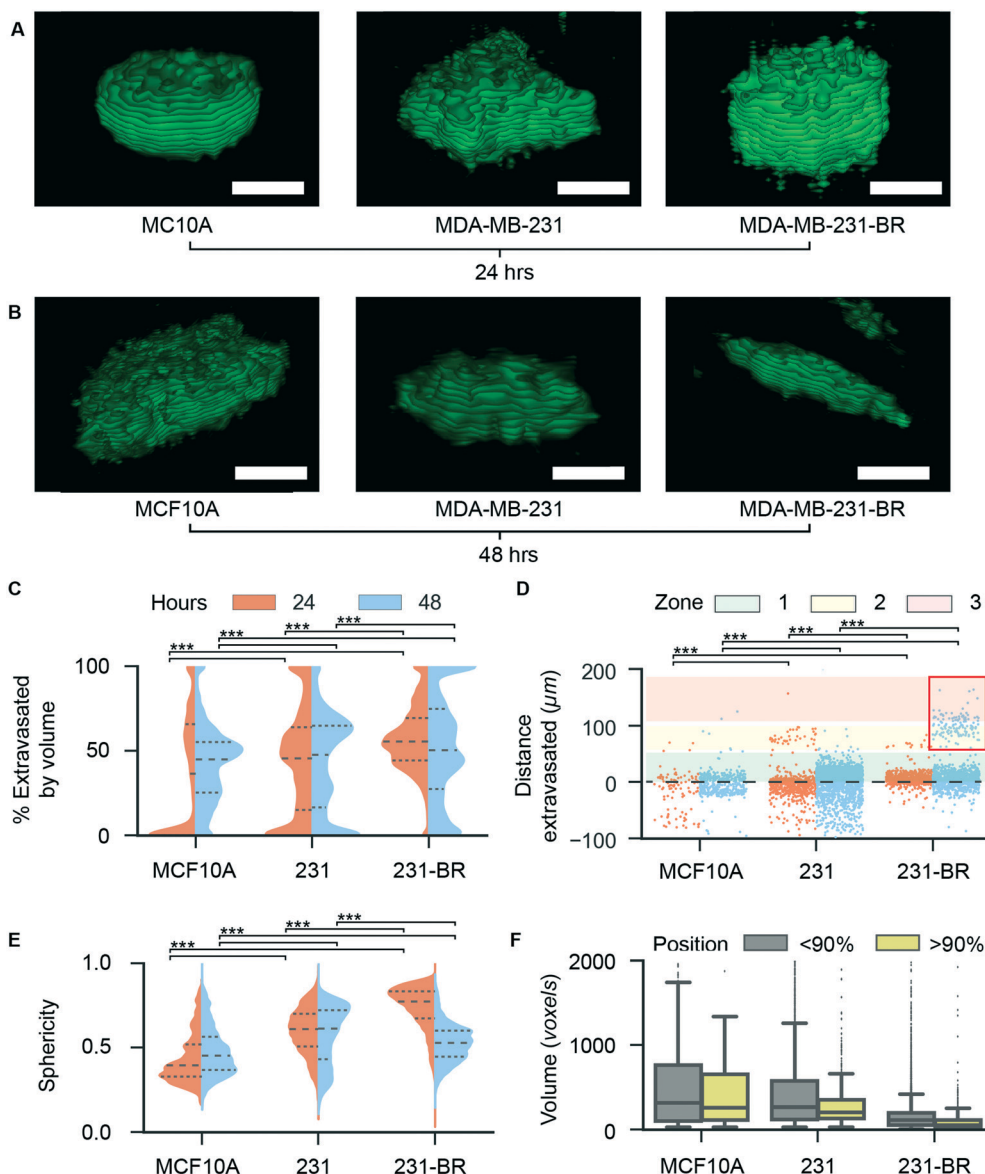


Fig. 3 Differences in extravasation and morphology of brain-seeking cells compared to non-brain-seeking cells in the μ BBN device analyzed using confocal tomography. (A) Representative images of morphology of cells in device. Scale bar = $\sim 25 \mu\text{m}$. (B) Representative images of morphology of cells in device at 48 h. Scale bar = $\sim 25 \mu\text{m}$. (C) Violin plot of percent total volume of cells extravasated through endothelial plane at 24 (orange) and 48 h (light blue). Dashed lines represent quartiles, longer dashed line represents the mean. (D) Strip plot of distance in μm of cancer cell centroids from plane at 24 and 48 h. (E) Violin plot of sphericity of cancer cells in μ BBN device at 24 and 48 h. Sphericity ranges from 1: spherical to 0: not spherical. (F) Plot of volume of each cell line in μ BBN device in voxels for cells $<90\%$ and $>90\%$ extravasated. *** $p < 0.0001$ for 24 h timepoint, *** $p < 0.0001$ for 48 h timepoint.

subpopulation of cells ($>90\%$ extravasated through the barrier) differed in size from those that interact with but did not traverse through the BBB. Illustrating this point, the MDA-MB-231-BR cells that extravasated were 58% smaller than those that did not (Fig. 3f, Table S2[†]).

Cancer and normal cell lines characterized by the system revealed a significant dynamic range of behaviors when encountering the BBB. Morphological differences of the brain metastatic cells measured over time suggest that cytoskeletal plasticity may contribute to successful extravasation. Given that MDA-MB-231-BR cells extravasated significantly between

24 and 48 h (Fig. 3c and d) and also exhibited a distinct shift from high to low sphericity (Fig. 3e), these data strongly support that the cytoskeletal plasticity necessary to adopt a spherical shape during extravasation enables the brain-seeking cells to traverse the endothelial layer more easily, and once within the brain niche, the cells become elongated to initiate colonization. This method of spherical extravasation has been reported previously by Allen *et al.* 2017 in contrast to the elongated extravasation of leukocytes.²¹ It is possible that smaller cells are better able to traverse the endothelial layer, as the cytoskeleton would have less distortion in shape and fewer tight

Table 1 Comparison of methods to classify cancer cells and PDX cancer cells by brain met potential

Cancer cells			
Method	AUC	CA	F1
Neural network	0.951	0.871	0.871
AdaBoost	0.950	0.876	0.876
Random forest	0.946	0.874	0.874
Tree	0.917	0.843	0.839
kNN	0.868	0.787	0.776
Logistic regression	0.848	0.779	0.783
Naïve Bayes	0.833	0.751	0.757
SGD	0.774	0.774	0.778
PDX Cancer cells			
Method	AUC	CA	F1
Neural network	0.972	0.881	0.878
Random forest	0.964	0.888	0.887
AdaBoost	0.957	0.881	0.879
Tree	0.954	0.867	0.865
Logistic regression	0.897	0.832	0.831
Naïve Bayes	0.896	0.846	0.849
kNN	0.882	0.818	0.814
SGD	0.861	0.860	0.853

junctions would need to be disrupted. The changes in sphericity observed in our system are consistent with a report by Sanz-Moreno *et al.* in which they note the role of actomyosin contractility as a means used by neoplastic cells to squeeze through voids in a 3D matrix.²² We find the propensity of the brain-seeking tumor cells to transition from spherical to non-spherical cell shapes to be a distinctive feature of the population that successfully extravasates through the membrane.

PDX-derived brain metastatic and primary tumor cells display differential phenotypic behaviors

It was unknown if patient-derived xenografts (PDXs) would survive and colonize the BBB niche. To demonstrate applicability of the system to patient's cells, we measured the differential behavior of various first-generation patient-derived-xenografts (PDXs). We profiled triple negative breast cancer (TNBC) from a primary tumor site (PDX9040C1), as well as triple-negative breast (PDXbrC1), lung (PDXLuC1), ovarian (PDXOvC1), and tongue PDX's (PDXTonC1) developed from brain metastatic sites of those diverse primary tumor types. Fig. 4a and b show examples of morphologies (low and high sphericity) of representative cells in the device for each cancer cell type.

The primary breast cancer PDX (PDX9040C1) had 87% and 79% of cells that were less than 50% extravasated after seeding at 24 and 48 h, respectively. However, in contrast, a much higher proportions of extravasated cells were observed from the PDXs derived from brain metastatic sites: 66% for breast PDXbrC1, 75% for lung PDXLuC1, 58% for ovarian PDXOvC1, and 92% for tongue PDXTonC1. Of the brain metastatic breast cancer PDX cells, more than 50% had extravasated at 24 h and ~4/5 (82%) had extravasated by 48 h (Fig. 4c). The mean, median, and standard deviation of percent volume extravasated

were calculated for each PDX and are reported in Table S3†. The distribution the % extravasated for each PDX sample differed significantly (p -values $< 0.05 \times 10^{-7}$) (Table S3†).

The distance the PDX cancer cells extravasated into the device (Fig. 4d) also differed between PDX samples, with PDXbrC1 and PDXTonC1 samples extravasating deepest into the device at 129 μm and 145 μm , respectively, at 24 h. This is 2.8-fold deeper than the primary (PDX9040C1) sample. Using the zone measurements defined above, PDX9040C1 had 34% of cells in Zone 1 at 24 h. Only 0.3% of these cells traveled beyond Zone 1. In sharp contrast, the brain metastatic PDXbrC1 and PDXTonC1 had a 4.6-fold and 59.0-fold larger proportion of cells beyond Zone 1 and had 0.7% and 1.4% of cells that travelled into Zone 3. No PDX9040C1 cells travelled into Zone 3 at 24 or 48 h. Moreover, in the PDXbrC1 samples, 87% of cells extravasated across the membrane in contrast to 35% in the PDX9040C1. PDXOvC1 did not migrate into the bottom chamber (>99%), remaining instead clustered near the endothelial layer. The distribution of cancer cell positions was significantly different between the brain metastatic and primary tumor PDX samples, with $p < 0.05$.

The morphologies of the PDX cells in the device were also measured by calculating the sphericity index of cells in the device over time (Fig. 4e). Similar to the previous results, the primary breast cells (PDX9040C1) maintained their sphericity level between 24 and 48 h (0.52 and 0.51). The brain metastatic breast cells (PDXbrC1) shifted from more spherical to less spherical between 24 and 48 h (0.64 to 0.53). Of the other sites of origin, lung (PDXLuC1) was the least spherical (0.53) while ovarian (PDXOvC1) was the most (0.61). Like the breast cell lines, the distribution of sphericity of PDXbrC1 cells showed two distinct populations, unlike the cells of PDX9040C1. Moreover, cells that have traversed into the brain stromal like space (those which have a percent volume extravasated >90%) showed decreased sphericity, except for the primary tumor cells. The volumes of cells that traversed the barrier had smaller volumes (Fig. 4f, Table S4†). For example, PDX9040C1 and PDXLuC1 that traversed the barrier were on average 59% and 80% smaller than the rest of the population.

First, we observed that the PDX cells from various primary locations survive and thrive in the *in vitro* human blood brain niche system which has not been shown previously. Primary human cells are known to be more sensitive to their environment and it has not been verified that an *in vitro* system can produce viable cultures. Moreover, the fact that the patient primary breast and breast brain metastasis mimic the behavior of the cancer cell line *in vitro* is remarkable. Finally, it is important to observe that the brain metastatic PDX cells show differential phenotypes that suggest data will be needed from many primary tumors to fully train an AI system to work across cancer types.

Brain metastatic cancer cells degrade the endothelial barrier

We measured each cell line in the μBBN device for nine days to observe if the cancer cells developed into pre-

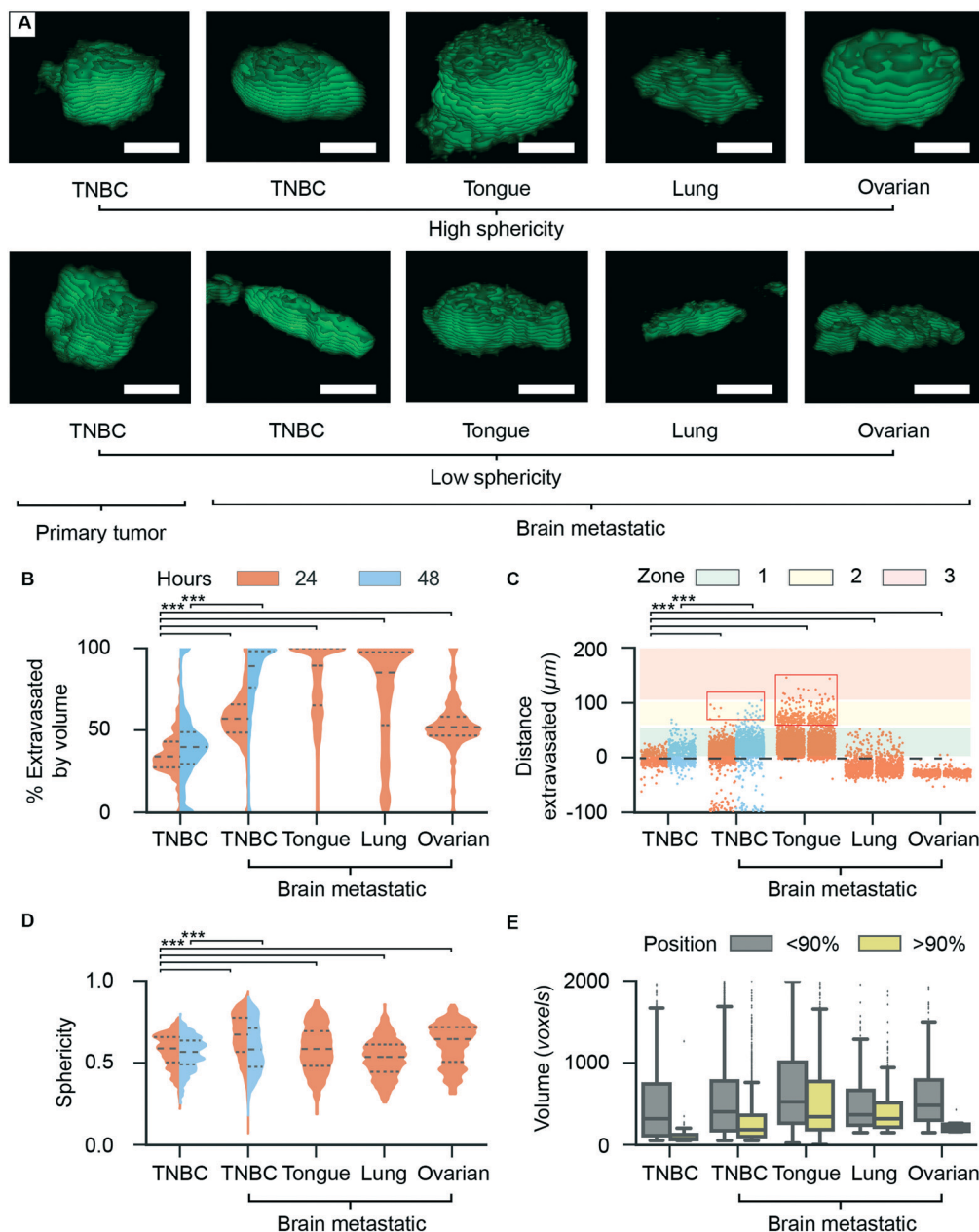


Fig. 4 Profiling of patient derived xenografts in μ BBN device. (A) Representative images of morphology of PDX cells in device with low and high sphericity. Scale bar = 25 μ m. (B) Violin plot of percent total volume of cells extravasated through plane for PDXs. (C) Strip plot of distance in μ m of PDX cell center from the endothelial layer. (D) Violin plot of sphericity of PDX cells in μ BBN device. (E) Box and whisker plot of volume PDX cells in μ BBN device in voxels for cells <90% and >90% extravasated *** p -value < 0.05.

colonization clusters and how they interacted with the cellular components of the μ BBN device. Fig. 5 shows that unlike normal-like breast cells which allow the endothelium to continue to proliferate and become more dense, cancer cells drastically degrade the endothelial barrier over time. Moreover, brain-seeking MDA-231BR cells reduced the coverage of the endothelium to a greater degree than the parental MDA-231 cells (Fig. 5b). Barrier degradation by cancer cells was observed concomitant with a marked increase in the number and organization of cancer cells in the stromal space (Fig. 5a and c).

The majority of cells consistently clustered near the endothelium after extravasation instead of migrating far into the brain microenvironment and this is consistent with *in vivo* reports.²³ From our data, we pose that metastatic cells may preferentially remain near the barrier to 1) de-regulate the barrier tight junctions and amplify the number of barrier traversing cancer cells, and/or 2) promote angiogenesis and redirection of the endothelial cells to support tumor colonization of the metastatic site. These hypotheses are supported by the observed drastic degradation of the endothelium (Fig. 5) by the colonizing brain seeking cells. While the data

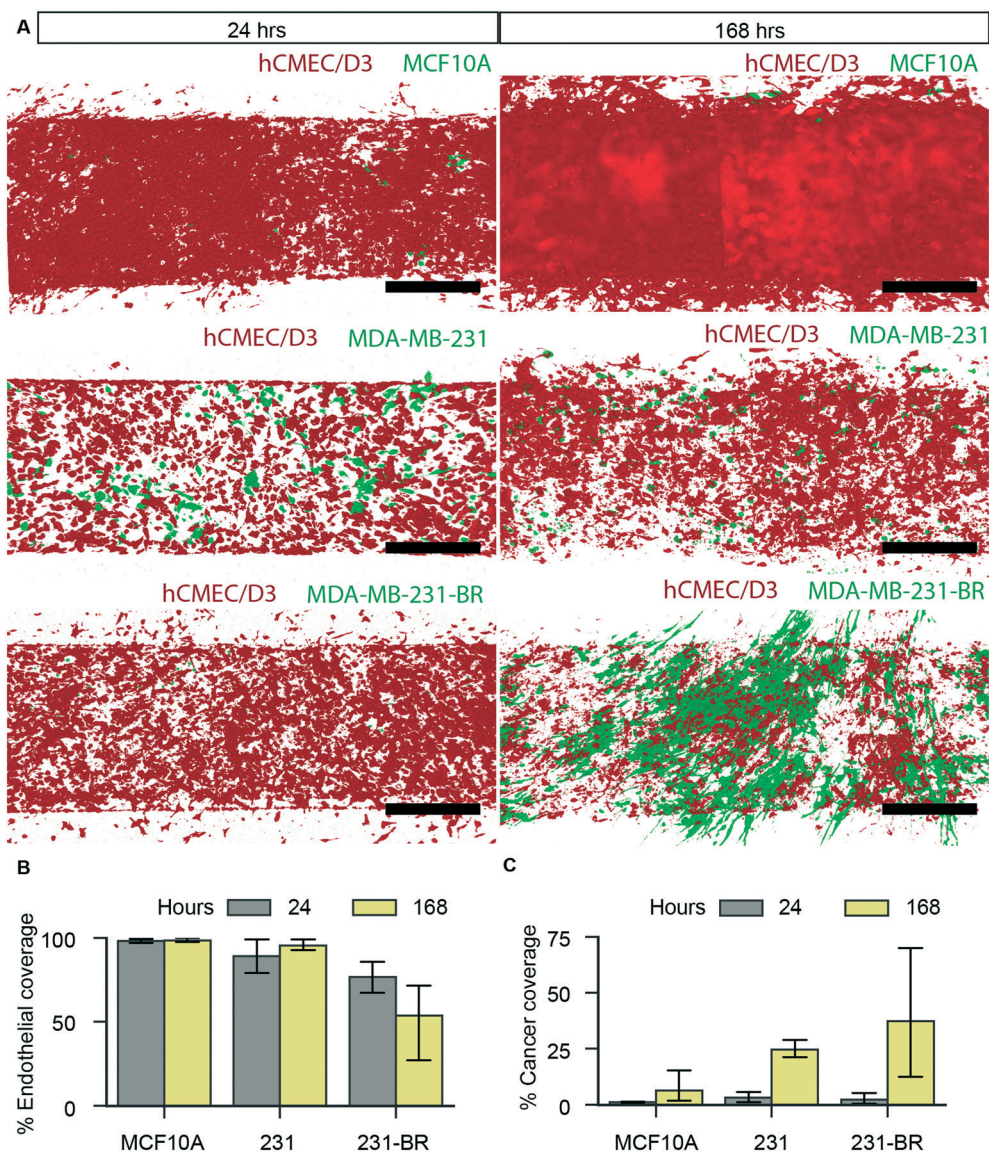


Fig. 5 Cancer cell interaction with the μ BBN endothelium. (A) Comparison of cell line degradation of the endothelium over 7 d (168 h) after adding the breast cells. The left and right panel shows cancer cells (green) and endothelial cells (red) 24 h and 7 d after seeding the cancer cells respectively. (B) Comparison of the endothelial coverage at 24 h and 168 h by cell line. (C) Comparison of cancer cell coverage as a percentage of area in the channel at 24 h and 168 h. Scale bar = 400 μ m.

indicate that aggressive cells may remain near the barrier, it does not account for potential repair mechanisms of the barrier that may occur after tumor colonization. This means that the window for therapeutic efficacy, especially for large molecule drugs, may be small, if the barrier will undergo repair after extravasation of the cancer cells.

Comprehensive differential cancer cell behavior *in vitro* leads to an index of brain metastatic potential

An important goal of this study was to confirm if the phenotypic expression of the cancer cells in the platform would enable the identification of cancer cells that had shown *in vivo* brain metastatic potential. From the results obtained above we realized that simply crossing the barrier (yes/no) is not

the only measurement needed to identify the cells with brain metastatic potential. An analysis, of the data using simple linear models produced poor results, therefore to evaluate the potential of the proposed method to identify cancer cells capable of colonizing the brain based on their behavior in an *in vitro* BBB, we applied a type of AI termed machine learning to generate an index corresponding to the probability a cell was derived from a brain metastatic clone. This model was developed in stages. First, we characterize the physical characteristics of cells described above in the process of traversing the BBB and discern the features of cells that traverse the BBB. The predictive power of the algorithm then, depended on its ability to predict if cancer cell subclones not previously encountered would traverse the BBB in a specific way. The traversal behavior of these new cells was confirmed *in vivo*

for cancer cell lines. Ten machine learning algorithms (Tables 1 and S5†) were investigated which produce a probabilistic value (0–1%) of high metastatic potential. The models were trained and cross-validated using the phenotypic behavior of the cells measured previously according to the workflow shown in Fig. 6a. The machine learning methods we investigated include Naive Bayes, random forest, tree, logistic regression, *k*-nearest-neighbor (*k*NN), stochastic gradient descent, neural network and Adaboost (random forest) (Table 1). To compare the methods, we scored them using three statistics: the area under the curve (AUC), accuracy (CA), and the weighted average of precision and recall (F1). When used in tandem these statistics provide insights into the performance and types of errors that the models may make when measuring a cells metastatic potential.²⁴ The top three performing methods according to their AUC were the neural network (AUC = 0.95), AdaBoost (random forest) (AUC = 0.95), and the random forest (AUC = 0.95) (Fig. 6b).

Important translational metrics are the positive predictive value (PPV) and negative predictive value (NPV). Both the PPV and NPV are 0.87 (Table S6†), which is generally considered excellent in predictive models of a clinical behavior, and of metastatic behavior in particular.

The same models were tested on patient derived xenografts (PDX) taken from brain metastasis to determine if brain metastatic cells could be differentiated from primary tumor cells, under the expectation that the performance would be likely to degrade due to their heterogeneity (Tables 1 and S7†). The brain metastatic PDX cells were de-

finied as the metastatic cells and the primary breast cancer PDX cells were defined as a non-brain metastatic control. The data measured in the chip was used to test the ability of the system to predict if cells in the chip belonged to the brain metastatic or non-brain metastatic cell type using the metastatic potential index (Tables 1 and S7†). This was done using the training performed on the cancer cell lines and a fresh training set taken from the PDX data. Moreover, this technique could identify between the different tumors of origin. The top three performing methods were the neural network (AUC = 0.97) followed by the random forest (AUC = 0.96) and AdaBoost (random forest) (AUC = 0.96) (Fig. 6c, Table 1). The resulting positive probability value (PPV) and negative probability value (NPV) are 0.91 and 0.85, respectively (Table S8†), indeed defying the *a priori* prediction that these parameters were likely to decrease, as heterogeneity increased.

There is a need for robust diagnostics that predict the future occurrence of brain metastasis from breast or other cancers at the time of primary diagnosis. In addition to the study, imaging tools are being tested for this application. Yin *et al.* has shown that MRI of brain composition can predict the number of days until brain metastases for non-small cell lung cancer, with accuracy, sensitivity, and specificity of 70%, 75%, and 66%, respectively.²⁵ Graesslin *et al.* reported on a model to predict brain metastasis for patients with metastatic breast cancer with an area under the curve (AUC) of 0.74.²⁶ A limitation of these methods is that the patient's brain must have undergone a change prior to diagnosis and is therefore, already susceptible to metastasis. Thus, a more direct

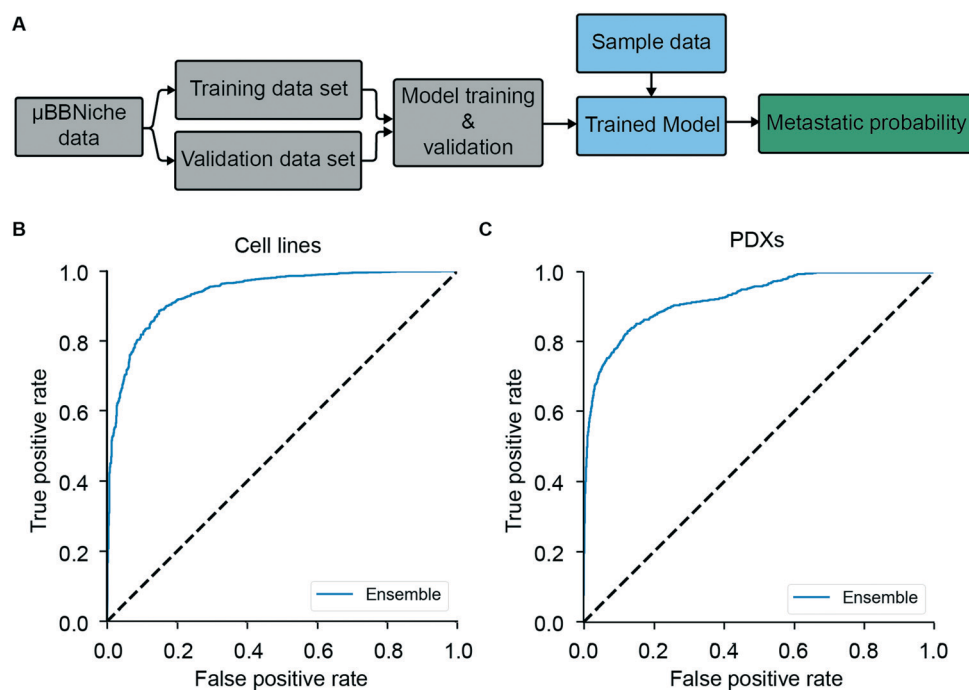


Fig. 6 Accurate identification of brain metastatic potential in μ BBN device. (A) Schematic of model development process. This process is divided into a training (grey) and testing (light blue) phase that outputs a probability a cell has a high metastatic potential (green). (B) Receiver operating characteristic (ROC) curve for the AdaBoost classification methods for cell lines. Upper left corner indicates good classification accuracy. (C) ROC curve for the AdaBoost classification methods for PDX samples.

approach which measures the behavior of a patient's primary cells in a brain environment, with increased accuracy and at a lower cost would be attractive. In this context, the results, support the measurement power of the system to predict the behavior of the cancer cells themselves. The low cost and quick turnaround time (24–48 h) of the μ BBN device along with the demonstrated ability to identify cancer subclones that then metastasized to the brain in murine models, make the device an excellent candidate to meet this technological gap. We acknowledge more study is necessary to optimize the brain micro-environment in the device which is a known area of active study in the field.^{27–30} Devices are being developed to include flow, additional cell types and improved barrier function overcoming the limitations of hCMEC endothelial cells. Regardless, we chose a realistic, simple and well understood model BBB employing the widely used hCMEC that was available at the start of the study to guide development of the imaging algorithm and AI components of the platform and the results are a positive contribution to the field. Moreover, the system identified patient derived cells based on their site of origin and previously known brain metastatic state, even though we tested a limited number of diverse PDXs. Future work expanding the library of PDX cells matched with knowledge of the patient outcomes would be the basis of a clinically usable training set. Taken together, this device could be further developed to identify cancer patients that may require additional screening and, as available, personalized treatment strategies to minimize the probability of brain metastasis.

Experimental section

Study design

The primary hypothesis investigated in this study were to (i) verify that cancer cells cultured *in vitro* mimic known *in vivo* behavior and (ii) establish that the behavior was distinct to brain metastatic cells and could be exploited as a diagnostic. The experiments presented were designed to compare first established lines with known brain seeking subclones and then to follow up with patient cells from biopsied tumors. All data presented are the result of three independent biological replicates with three technical replicates performed for each, but each measurement includes hundreds of cells.

μ m-blood brain niche design and validation

The complex series of processes by which a cancer cell moves from the primary tumor site to distant sites is known as the metastatic cascade.^{31–34} Initially, cancer cells invade into the tissue around the primary site. The cells then intravasate into the bloodstream where they may survive in the circulatory system until they adhere to the endothelium at a distant site. In the case of brain metastasis, the cells extravasate through the BBB endothelium where they then colonize and grow within the brain stroma. The μ BBN device (Fig. 2a and b) was designed to study the late and most definitively clinically impactful steps of the brain metastatic cascade: adherence, ex-

travasation, and colonization. It is based on previously published and accepted models such as the one by Wang *et al.*, Marino *et al.*, Esch *et al.*, and Chen *et al.*^{35–38}

The μ BBN we designed, is composed of two chambers separated by a 5 μ m microporous membrane (Fig. 2b and S1†). The device is fabricated from polydimethylsiloxane (PDMS) because of its inertness during cell culture. The upper chamber mimics the brain vasculature with a lining of human cerebral microvascular endothelial cells, hCMEC/D3. The lower chamber is filled with hTERT immortalized normal human astrocytes (NHA) suspended in a type I collagen matrix. The porous membrane is sized to separate the upper and lower chambers without obstructing the inlets and outlets. After various pilot trials, we chose 5 μ m pore membranes to optimize three functions: support for the endothelial layer, ease of extravasation, and clarity of imaging. Micropipette tips are placed in each inlet/outlet port to serve as medium reservoirs and facilitate easy loading of liquids and cells. The assembled chip is bonded to a 50 mm \times 75 mm glass slide and positioned using an alignment fixture (Fig. 2c). This chip has four independent sets of chambers imprinted on it for ease of replication of each experiment.

To use the engineered brain niche to study cancer cell extravasation, we first validated the barrier function of the human cerebral microvascular endothelial cell (hCMEC/D3) monolayer in the device. The hCMEC/D3 cells formed a monolayer in the upper channel over a 3 day period post-seeding (Fig. S4b†). Co-culture of the astrocytes and endothelial cells required that their respective media be mixed at a 50 : 50 ratio to promote simultaneous healthy growth of both cell lines and barrier formation (Fig. S2†). The endothelial barrier permeability was characterized using FITC-Dextran exclusion.

Small molecule membrane transfer measurements

We conducted a FITC-Dextran exclusion assay in which 10 kDa FITC-Dextran was introduced to the upper chamber. Diffusion of the dye was measured over 24 h using the relative fluorescence intensity (RFI) approach (Fig. 2f and g). The intensity of the region measured was plotted as a percentage of the normalized intensity of a calibration solution of FITC-DEX.³⁹ There was an increase in dye content over the first hour in the lower chamber, in line with other models in the literature,³² with a maximal RFI of 4% followed by a stable diffusion (Fig. 2g). In contrast, the diffusion was significantly higher, with a maximal RFI of 74% ($p < 0.05$) when no endothelial layer was present.

FITC-Dextran conjugated dye (Sigma-Aldrich, CAS: 60842-46-8, 5 mg ml⁻¹, 10 kDa) was used to assess total integration fluorescence of small molecules across the endothelial layer in the device. Images were taken using an inverted fluorescent microscope with a 10 \times objective. The fluorescent signal at the interface between the upper and lower chamber was measured at 1, 5, 10, 20, 60 and 1440 minutes. Three images were taken at the interface between the upper and lower chamber at three pre-determined locations along the device

(center, 5 mm from top and 5 mm from bottom) for three channels and $n = 3$ biological replicates.

Cell culture and reagents

MCF10A (ATCC CRL-10317) cells were maintained in 50:50 DMEM:F12 medium (Corning 10-090-CV) supplemented with 5% horse serum, $10 \mu\text{g ml}^{-1}$ insulin, $0.5 \mu\text{g ml}^{-1}$ hydrocortisone, $0.02 \mu\text{g ml}^{-1}$ epidermal growth factor, $0.1 \mu\text{g ml}^{-1}$ cholera toxin, and 5 mL antibiotic-antimycotic (Gibco 15240062). MCF10A cells were stained using Cell Tracker Green according to the manufacturer's protocol. MDA-MB-231 and MDA-MB-231-BR-GFP cells were obtained from Patricia Steeg, PhD and were maintained in DMEM (Corning 10-013-CV), supplemented with 10% FBS and 5 mL antibiotic-antimycotic (Gibco 15240062). hCMEC/D3 (EMD Millipore SCC066) cells were maintained in EGM-2 medium (Lonza CC-3162). MDA-MB-231-GFP fluorescent cells were created by transfecting MDA-MB-231 cells with empty vector pLLEV-GFP lentivirus. hCMEC/D3-DsRed fluorescent cells were created by transfecting hCMEC/D3 cells with empty vector pLL 3.7-dsRed lentivirus. Normal human astrocytes (NHA) were obtained from Lonza (CC-2565) and were immortalized using lentiviral induced hTERT expression and were maintained in AGM media (Lonza CC-3186). Lentivirus was created using pLOX-TERT-iresTK lentiviral vector obtained from Addgene (12245) and packaging vectors psPAX2 and pMD2.G also obtained from Addgene (12260 and 12259) in HEK-293 T cells. Cells were grown at 37°C in 5% CO_2 .

Patient derived xenografts

Human tumor tissue was collected at the University of Michigan under approved IRB protocols at University of Michigan. Animal studies were performed under approved University of Michigan institutional animal care and use committee (IACUC) protocols.

Freshly resected human tumor tissue was immediately and directly implanted into eight-week-old NSG mice (Jackson lab). Breast tumor tissue was implanted into the mammary fat pad and non-breast tumor tissue was implanted into both flanks. Tumor growth was monitored once a week and were harvested when the tumor size reached 0.6–0.7 cm.

Excised tumors were cut into 2–4 mm pieces and dissociated to single cell suspensions using a gentle MACS dissociation platform (Miltenyi Biotec) according to the manufacturer's protocol. The single cell suspensions were counted using a hemacytometer, then resuspended in $80 \mu\text{L}$ of 1X PBS, pH 7.4 supplemented with 0.5% BSA and $20 \mu\text{L}$ of mouse cell depletion cocktail (cat# 130-104-694) containing magnetically labeled antibodies per 107 cells. Samples were incubated at 4°C for 15 minutes then applied to a LS column to deplete the magnetized mouse cells from the purified human tumor cells. The purified human tumor cells were then stained with Cell Tracker Green according to the manufacturer's protocol, then counted using a hemacytometer before use.

Live subject statement

All human tissues were collected from patients treated at Michigan Medicine, who provided written, in-person informed consent under a protocol approved by the University of Michigan Institutional Review Board (IRB).

Seeding microfluidic device

The bottom chamber of the devices was seeded with 1×10^6 NHA suspended in a solution of 1 mL of 3 mg mL^{-1} PureCol type I bovine collagen with $128 \mu\text{L}$ 0.8 M NaHCO_3 and $40 \mu\text{L}$ 10X high-glucose (250 mM) DMEM and incubated at 37°C for one hour. The top chamber was coated with 2% growth-factor reduced Matrigel in AGM and incubated at 37°C for one hour. hCMEC cells were seeded in the top chamber by pipetting $30 \mu\text{L}$ of cells at 1 million cells per mL in 50:50 AGM/EGM-2 in both inlet and outlet twice, with 15 min between each inoculation. Devices were then incubated at 37°C and 5% CO_2 , changing media in both chambers every 12 h. Cancer and normal-like cells were seeded into the top chamber inlet of a confluent device at a density of 3×10^4 cells.

Measurement of the cell attributes using confocal tomography

Extracting meaningful data from images of the organ-on-a-chip device poses a major challenge. Thus, we developed software based on the Visualization tool kit (VTK) library, termed confocal tomography, to measure the extravasation behavior of cancer cells relative to the endothelial layer.²⁰ In brief, the algorithm fits a 2D surface to the endothelial layer using the centers of the cells (centroids) as points on the plane. Then, each cancer cell is converted from the confocal z-stack into a 3D object. Each 3D cancer cell object is then compared to the endothelial layer plane to measure the cell's morphological and functional metrics. To calculate the percent volume of the cell that has extravasated across the endothelial plane the cells 3D mesh is cut using a Boolean operation and the resulting hole closed to divide the cell into two bodies. A representative result of these measurements is shown in Fig. 2e.

Sphericity was measured by comparing the volume and area of the cell, the ratio of which may deviate from a perfect sphere according to the equation below:

$$S = \frac{\pi \frac{1}{3} \left(6V^{\frac{2}{3}} \right)}{A}$$

Statistical analysis

Analysis was performed using Python and R Studio. Comparisons of populations of cells were made using a Smirnov–Kolmogorov test and Kruskal–Wallis Rank Sum Test with a p -value test at 0.05. The double-sided t -test was used to compare the means of the RFI results for μBBN chips with an

endothelial and no-endothelial layer. The means of the cell area coverage in Fig. 4 and 5 were tested using a Kruskal–Wallis test and if significant also by a pairwise comparison Tukey and Kramer (Nemenyi) test.

Artificial intelligence machine learning algorithm

Binary classification was performed in Orange (Fig. 6a). The data was filtered to remove bad measurements, defined as those that failed a Boolean operation or giving parametric variable values outside of known bounds (−100–200, 0–1 and 0–2000). Using the cell lines as an example the MDA-MB-231-BR-GFP cells were labeled as brain metastatic and the remaining cell lines were labelled as non-brain metastatic. The features used to classify cells included all parametric variables. The data was sampled into a training (80%) and test set (20%). The training set was stratified and cross-validated using 10 folds against each model/classifier. The models/classifiers studied included neural network, Naïve Bayes, random forest, tree, logistic regression, *k*NN, stochastic gradient descent and AdaBoost latched to random forest. After training the data the test data was used to score the performance of the model by classifying the cells in the chip according to the probability, they were in the brain metastatic cell line from 0 to 1. The model performance was ranked according to the area under the curve (AUC) of the ROC, the accuracy and the F1 score. When used in tandem, these statistics provide insights into the performance and types of errors that the models may make when measuring a cell's metastatic potential.²⁴

Breast (cancer) cell lines

All laboratory Breast cell lines (MCF10A, MDA-MB-231) used in this research have been authenticated *via* ATCC's STR profiling service prior to fluorescent labelling.

Conclusion

In conclusion, we presented the development and potential of a platform designed to identify the subtle phenotypic differences between cancer cells that show brain metastatic behavior and those that do not, based on their behavior in a brain like tumor micro-environment with potential for translation to the clinic as a brain metastatic predictive diagnostic given additional study. The method was validated by measuring the extravasation and metastatic events of breast cancer cells and PDX cancer cells in the device. Future work will expand the library of patient samples used to train the system to improve its clinical applicability. Additional work will use the device to evaluate the molecular determinants of the migration, survival of metastatic cancer cells and to test the efficacy of potential new treatments on metastatic cancer within the brain niche.

Funding

Work was supported by: NIH T32CA009676 (CRO, MA), the University of Michigan Rogel Cancer Center Nancy Newton

Loeb Fund (MA), by NIH grants P30CA046592 (BL, SDM, MA, CRO), CA196018 (CRO, ST), AI116482 (CRO, ST), by the METAvivor Foundation (MA, SDM) and the Breast Cancer Research Foundation (CRO, SDM).

Author contributions

Conceptualization: S. D. M., C. R. O., B. L., M. A., M. C., A. M., S. T. Methodology: C. R. O., M. A., B. L., M. D. Software: C. R. O. Validation: formal analysis: C. R. O., K. K. Investigation: C. R. O., M. A. B. L., T. W., H. C., J. Y. Resources: X. C., S. D. M., M. A., M. D., Z. W., A. M., J. H. Data curation: C. R. O. Writing – original draft: C. R. O., M. A., T. W. Writing – review & editing: S. D. M., M. C., S. T., A. M., J. Y. Visualization: C. R. O., M. A. Supervision: S. D. M., S. T. Funding acquisition: S. D. M., C. R. O., M. A.

Conflicts of interest

There are no conflicts to declare.

Acknowledgements

We thank the Steeg Lab, at the National Cancer Institute for the generous donation of MDA-MB-231-BR cells. Confocal microscopy was performed at the University of Michigan Biointerface Institute (BI). Flow cytometry was performed at the University of Michigan Flow Cytometry Core. Viral vectors were created by the University of Michigan Vector Core. We also thank Kelly Kidwell for guidance in statistical analysis of this data.

Notes and references

- 1 C. Aversa, *et al.* Metastatic breast cancer subtypes and central nervous system metastases, *Breast*, 2014, **23**, 623–628.
- 2 H. Kennecke, *et al.* Metastatic behavior of breast cancer subtypes, *J. Clin. Oncol.*, 2010, **28**, 3271–3277.
- 3 N. Niikura, S. Saji, Y. Tokuda and H. Iwata, Brain Metastases in Breast Cancer, *Jpn. J. Clin. Oncol.*, 2014, **44**, 1133–1140.
- 4 L. Nayak, E. Q. Lee and P. Y. Wen, Epidemiology of brain metastases, *Curr. Oncol. Rep.*, 2012, **14**, 48–54.
- 5 N. U. Lin and E. P. Winer, Brain metastases: The HER2 paradigm, *Clin. Cancer Res.*, 2007, **13**, 1648–1655.
- 6 P. R. Lockman, *et al.* Heterogeneous blood-tumor barrier permeability determines drug efficacy in experimental brain metastases of breast cancer, *Clin. Cancer Res.*, 2010, **16**, 5664–5678.
- 7 E. M. Olson, *et al.* Clinical outcomes and treatment practice patterns of patients with HER2-positive metastatic breast cancer in the post-trastuzumab era, *Breast*, 2013, **22**, 525–531.
- 8 G. Binning, R. Huss and G. Schmidt, *Tissue Phenomics: Profiling Cancer Patients for Treatment Decisions*, Pan Stanford, 2018.

- 9 B. J. Williams, *et al.* Digital pathology for the primary diagnosis of breast histopathological specimens: an innovative validation and concordance study on digital pathology validation and training, *Histopathology*, 2018, 72, 662–671.
- 10 S. Jha and E. J. Topol, Adapting to artificial intelligence: Radiologists and pathologists as information specialists, *JAMA, J. Am. Med. Assoc.*, 2016, 316(22), 2353–2354.
- 11 R. L. Schmidt, *et al.* Risk-benefit analysis of sampling methods for fine-needle aspiration cytology: A mathematical modeling approach, *Am. J. Clin. Pathol.*, 2013, 139, 336–344.
- 12 R. Meuwissen, *et al.* Induction of small cell lung cancer by somatic inactivation of both Trp53 and Rb1 in a conditional mouse model, *Cancer Cell*, 2003, 4, 181–189.
- 13 M. Kato, *et al.* The herbal medicine Sho-saiko-to inhibits growth and metastasis of malignant melanoma primarily developed in ret-transgenic mice, *J. Invest. Dermatol.*, 1998, 111, 640–644.
- 14 N. A. Oberheim, *et al.* Uniquely Hominid Features of Adult Human Astrocytes, *J. Neurosci.*, 2009, 29, 3276–3287.
- 15 K. K. Shah, L. Yang and T. J. Abbruscato, In vitro models of the blood-brain barrier, *Methods Mol. Biol.*, 2012, 814, 113–128.
- 16 B. Prabhakarandian, *et al.* SyM-BBB: a microfluidic blood brain barrier model, *Lab Chip*, 2013, 13, 1093.
- 17 R. Booth and H. Kim, Characterization of a microfluidic in vitro model of the blood-brain barrier (μ BBB), *Lab Chip*, 2012, 12, 1784–1792.
- 18 Q. T. Ostrom, *et al.* NEURO-ONCOLOGY CBTRUS Statistical Report: Primary Brain and Central Nervous System Tumors Diagnosed in the United States in 2006–2010, *Neuro-Oncology*, 2013, 12, 28–36.
- 19 N. Niikura, *et al.* Treatment outcomes and prognostic factors for patients with brain metastases from breast cancer of each subtype: a multicenter retrospective analysis, *Breast Cancer Res. Treat.*, 2014, 147, 103–112.
- 20 W. J. Schroeder, L. S. Avila and W. Hoffman, Visualizing with VTK: A tutorial, *IEEE Comput. Graph. Appl.*, 2000, 20, 20–27.
- 21 T. A. Allen, *et al.* Angiogenesis as an alternative mechanism of cell extravasation, *Stem Cells*, 2017, 35, 170–180.
- 22 V. Sanz-Moreno, *et al.* Rac Activation and Inactivation Control Plasticity of Tumor Cell Movement, *Cell*, 2008, 135, 510–523.
- 23 A. F. Eichler, *et al.* The biology of brain metastases—translation to new therapies, *Nat. Rev. Clin. Oncol.*, 2011, 8, 344.
- 24 M. Sokolova and G. Lapalme, A systematic analysis of performance measures for classification tasks, *Inf. Process. Manage.*, 2009, 45, 427–437.
- 25 G. Yin, *et al.* Predicting brain metastases for non-small cell lung cancer based on magnetic resonance imaging, *Clin. Exp. Metastasis*, 2017, 34, 115–124.
- 26 O. Graesslin, *et al.* Nomogram to predict subsequent brain metastasis in patients with metastatic breast cancer, *J. Clin. Oncol.*, 2010, 28, 2032–2037.
- 27 E. A. L. M. Biemans, L. Jäkel, R. M. W. de Waal, H. B. Kuiperij and M. M. Verbeek, Limitations of the hCMEC/D3 cell line as a model for A β clearance by the human blood-brain barrier, *J. Neurosci. Res.*, 2017, 95, 1513–1522.
- 28 Y. P. Choi, *et al.* Cancer-associated fibroblast promote transmigration through endothelial brain cells in three-dimensional in vitro models, *Int. J. Cancer*, 2014, 00, 1–10.
- 29 R. Van Horssen, N. Galjart, J. A. P. Rens, A. M. M. Eggermont and T. L. M. Ten Hagen, Differential effects of matrix and growth factors on endothelial and fibroblast motility: Application of a modified cell migration assay, *J. Cell. Biochem.*, 2006, 99, 1536–1552.
- 30 J. W. Song, *et al.* Computer-controlled microcirculatory support system for endothelial cell culture and shearing, *Anal. Chem.*, 2005, 77, 3993–3999.
- 31 D. Wirtz, K. Konstantopoulos and P. C. Searson, The physics of cancer: the role of physical interactions and mechanical forces in metastasis, *Nat. Rev. Cancer*, 2011, 11, 512–522.
- 32 J. A. Brown, *et al.* Recreating blood-brain barrier physiology and structure on chip: A novel neurovascular microfluidic bioreactor, *Biomicrofluidics*, 2015, 9(5), 054124.
- 33 Y. Takeshita, *et al.* An in vitro blood-brain barrier model combining shear stress and endothelial cell/astrocyte co-culture, *J. Neurosci. Methods*, 2014, 232, 165–172.
- 34 R. Booth and H. Kim, Characterization of a microfluidic in vitro model of the blood-brain barrier (μ BBB), *Lab Chip*, 2012, 12, 1784.
- 35 Y. I. Wang, H. E. Abaci and M. L. Shuler, Microfluidic blood-brain barrier model provides in vivo-like barrier properties for drug permeability screening, *Biotechnol. Bioeng.*, 2017, 114, 184–194.
- 36 A. Marino, *et al.* A 3D Real-Scale, Biomimetic, and Biohybrid Model of the Blood-Brain-Barrier Fabricated through Two-Photon Lithography, *Small*, 2018, 14(6), 1702959.
- 37 M. B. Esch, D. J. Post, M. L. Shuler and T. Stokol, Characterization of In Vitro Endothelial Linings Grown Within Microfluidic Channels, *Tissue Eng., Part A*, 2011, 17, 2965–2971.
- 38 M. B. Chen, J. A. Whisler, J. S. Jeon and R. D. Kamm, Mechanisms of tumor cell extravasation in an in vitro microvascular network platform, *Integr. Biol.*, 2013, 5, 1262.
- 39 L. Shi, M. Zeng, Y. Sun and B. M. Fu, Quantification of Blood-Brain Barrier Solute Permeability and Brain Transport by Multiphoton Microscopy, *J. Biomech. Eng.*, 2014, 136(3), 031005.